ADVANCED MATERIALS INTERFACES
Open Access
www.advmatinterfaces.de

Tuning the Permeation Properties of Poly(1-trimethylsilyl-1-propyne) by Vapor Phase Infiltration Using Trimethylaluminum

Jonathan Jenderny, Nils Boysen, Jens Rubner, Frederik Zysk, Florian Preischel, Teresa de los Arcos, Varun Raj Damerla, Aleksander Kostka, Jonas Franke, Rainer Dahlmann, Thomas D. Kühne, Matthias Wessling, Peter Awakowicz, and Anjana Devi**

Vapor phase infiltration (VPI) has emerged as a promising tool for fabrication of novel hybrid materials. In the field of polymeric gas separation membranes, a beneficial impact on stability and membrane performance is known for several polymers with differing functional groups. This study for the first time investigates VPI of trimethylaluminum (TMA) into poly(1-trimethylsilyl-1-propyne) (PTMSP), featuring a carbon–carbon double bond as functional group. Saturation of the precursor inside the polymer is already attained after 60 s infiltration time leading to significant densification of the material. Depth profiling proves accumulation of aluminum in the polymer itself, but a significantly increased accumulation is visible in the gradient layer between polymer and SiO_2 substrate. A reaction pathway is proposed and supplemented by density-functional theory (DFT) calculations. Infrared spectra derived from both experiments and simulation support the presented reaction pathway. In terms of permeance, a favorable impact on selectivity is observed for infiltration times up to 1 s. Longer infiltration times yield greatly reduced permeance values close or even below the detection limit of the measurement device. The present results of this study set a strong basis for the application of VPI on polymers for gas-barrier and membrane applications in the future.

1. Introduction

With a growing demand for high performance materials for advances in areas such as nano- and biotechnology or the energy sector, inorganic–organic hybrid materials are a popular choice, combining the advantages of both organic and inorganic materials. Application of these materials ranges from catalysis and tunable dielectrics to nanopatterning, photoresists, barriers, membranes, and improving materials' scratch resistivity.[1–7]

Important aspects in hybrid material synthesis involve surface functionalization and incorporation of inorganic material, e.g., nanoparticles in organic structures. Common techniques for the synthesis of thin films of such materials are sol–gel, chemical vapor deposition (CVD), atomic layer deposition (ALD) or molecular layer deposition (MLD).[8–10] For surface functionalization, e.g., in

J. Jenderny, P. Awakowicz
Applied Electrodynamics and Plasmatechnology
Ruhr University Bochum
44801 Bochum, Germany
E-mail: jonathan.jenderny@rub.de

N. Boysen, A. Devi
Fraunhofer Institute for Microelectronic Circuits and Systems (IMS)
47057 Duisburg, Germany
E-mail: anjana.devi@rub.de

The ORCID identification number(s) for the author(s) of this article can be found under https://doi.org/10.1002/admi.202400171

DOI: 10.1002/admi.202400171

J. Rubner, M. Wessling
Chemical Process Engineering AVT.CVT
RWTH Aachen University
52074 Aachen, Germany

F. Zysk, T. D. Kühne
Dynamics of Condensed Matter and Center for Sustainable Design
Chair of Theoretical Chemistry
Paderborn University
33098 Paderborn, Germany

F. Preischel, A. Devi
Inorganic Materials Chemistry (IMC)
Ruhr University Bochum
44801 Bochum, Germany

T. de los Arcos, V. R. Damerla
Technical and Macromolecular Chemistry
Paderborn University
33098 Paderborn, Germany

microelectronics, a thin film is often deposited. A conventional method to deposit such films with high precision and control is ALD,[9] often combined with MLD.[10] By adapting the ALD process to plasma enhanced ALD (PE-ALD)[11] or vapor phase infiltration (VPI)[12] a wider range of applications and materials can be accessed. In VPI processes, exposure time of the metal-organic precursor is prolonged compared to a conventional ALD process. This longer exposure time allows reactions of the precursor not only with surface near regions but also with the bulk material of the substrate.[13] Fundamentally, VPI processing consists of the following steps: First, the precursors dissolves into the substrate then diffusing through the material reacting with potential functional groups. In a following purging or precursor removal step, typically by evacuating the reactor, precursor molecules which have not yet reacted may desorb and leave the substrate material. Entrapment of precursor in the material is possible using a co-reactant, in most cases water vapor. This will lead to formation of for example metal oxide or metal hydroxides, depending on the type of co-reactant. In the field of polymeric gas separation membranes, it has been shown that by deposition of a thin selective layer, the membrane performance can be improved.[14,15] A common problem of such polymers, however, is their swelling when exposed to humid gases over prolonged times. In the context of polymeric gas separation membranes, swelling is known to increase the chain mobility of the polymer. This results in generally increased diffusion coefficients for all gases, thereby leading to an undesired reduction in selectivity.[16] Taha et al.[6] and Ahmad et al.[17] have reported that by incorporation of nanoparticles in the polymer, this phenomenon could be inhibited. When using VPI, this issue can be addressed alongside an increase in the membrane's performance as shown by McGuinness et al.[18] for the infiltration of polymer of intrinsic microporosity 1 (PIM-1) membranes with trimethylaluminum (TMA).

Transport of gases in dense, non-porous polymers is often described by a solution diffusion approach as outlined e.g., by Baker.[19] In essence, how well gases permeate through a given material is assumed to mainly depend on sorption and diffusion coefficients. As shown by Tanaka et al.,[20] diffusion coefficients are much more susceptible to changes of the membrane material compared to sorption coefficients. In this regard, VPI of TMA into polymers is believed to form an aluminum oxide network, similarly as reported by McGuinness et al.[18] for VPI of TMA into PIM-1. Presence of such an additional network within the material would limit diffusion and favor transport of smaller molecules. Additionally, changes in wettability of the inner volume could affect transport of condensable gases. Among different polymers used in gas separation applications, poly(1-trimethylsilyl-1-propyne) (PTMSP) stands out as a glassy polymer featuring exceptionally high gas permeability owing to its high free volume.[21] PTMSP is of potential interest for VPI via TMA to enhance the selectivity of the gas separation membrane by functionalization of the inner free volume of the PTMSP polymer. In addition, PTMSP is highly organic, featuring a carbon–carbon double bond as functional group. Up to now, no data has been published investigating the VPI via TMA into a polymer with this functional group. Furthermore, only little data is available on the tuning of permeation performance of PTMSP using surface or bulk chemical reactions after deposition of the initial PTMSP film. Based on the existing reports on VPI for polymeric gas separation membranes, a beneficial impact on PTMSP is assumed. First evidence is provided by Rubner et al.[22] reporting on the mitigation of PTMSP aging via plasma enhanced chemical vapor deposition of organosilicon coatings and by Pramanik and Regen[23] showing an increase in CO_2/N_2 selectivity when modifying the surface with a thiol-ene click reaction.

In this manuscript, the development of a VPI process of TMA into spin-coated PTMSP on SiO_2 and polyacrylonitrile (PAN) flat sheet membranes is shown for variation of infiltration temperature and TMA infiltration times. The infiltration is analyzed by quartz crystal microbalance (QCM) providing insights into net mass gain. Surface and structural changes are tracked by atomic force microscopy (AFM), ellipsometry, contact angle measurements, scanning transmission electron microscopy (STEM), and transmission electron microscopy (TEM). Depth profiling via X-ray photoelectron spectroscopy (XPS), time of flight secondary ion mass spectroscopy (TOF-SIMS) and energy-dispersive X-ray spectroscopy (EDS) is employed for evaluation of infiltration depth and depth dependent changes in stoichiometry. A reaction mechanism is proposed and validated by density functional theory (DFT) calculations supplemented by infrared (IR) spectra from experiments and simulations. Finally, the impact of infiltration on the polymer's porosity and free volume is evaluated using cyclic voltammetry (CV) and permeation measurements.

2. Results and Discussion

2.1. Infiltration Process

The solution for the PTMSP polymer is spin coated on oxidized silicon wafers and PAN flat sheet membranes. Thickness of the PTMSP coating was estimated using ellipsometry. PTMSP is known to change its internal structure and free volume over time, commonly referred to as aging.[21] Thus, PTMSP has to undergo a so called rejuvenation step prior to infiltration with TMA. The

A. Kostka
Center for Interface-Dominated High Performance Materials
Ruhr University Bochum
44801 Bochum, Germany
J. Franke, R. Dahlmann
Institute for Plastics Processing (IKV)
RWTH Aachen University
52074 Aachen, Germany
T. D. Kühne
Center for Advanced Systems Understanding (CASUS)
Helmholtz-Zentrum Dresden-Rossendorf
02386 Görlitz, Germany
T. D. Kühne
Institute of Artificial Intelligence
Chair of Computational System Sciences
Dresden University of Technology
01187 Dresden, Germany
A. Devi
Leibniz Institute for Solid State and Materials Research (IFW)
01069 Dresden, Germany
A. Devi
Chair of Materials Chemistry
Dresden University of Technology (TUD)
01069 Dresden, Germany

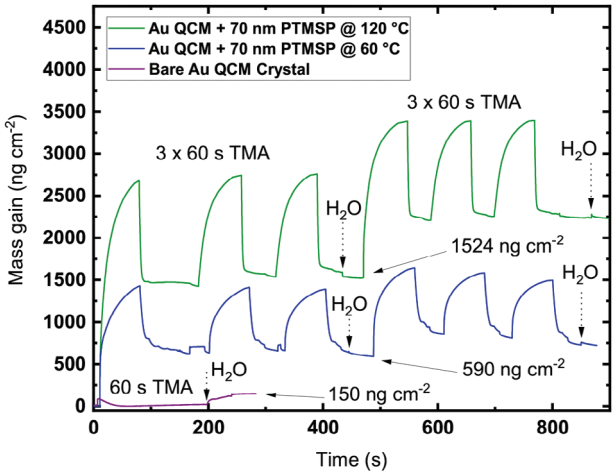

Figure 1. Mass gain during infiltration in the low pressure reactor of 70 nm PTMSP deposited on QCM crystals at 60 and 120 °C infiltration temperature. TMA is pulsed for 60 s followed by evacuation of the reactor. The application of a water pulse is marked by the dotted arrows. For the reference, one 60 s TMA pulse was analyzed followed by a water pulse. Both infiltrated samples were subject to three 60 s TMA pulses before application of a water pulse.

rejuvenation hereby aims to reinstate the original state of the polymer. Details on PTMSP preparation and rejuvenation are provided in the Experimental Section 4 following the procedure by Rubner et al.[22] Infiltration is performed in two different setups: i) a low pressure reactor (base pressure 10^{-5} mbar) already used for previous VPI studies[24] and ii) a high pressure reactor (base pressure 10^{-2} mbar). Infiltration in the low pressure reactor follows the procedure reported by Mai et al.[24] After positioning the sample in the reactor and subsequent evacuation, static vacuum conditions are used (i.e., the pumps are sealed off from the reactor during infiltration) to facilitate infiltration into the polymer. TMA is introduced into the chamber for the desired process time, followed by a vacuum purge to base pressure. Finally, a 1 s water pulse was applied to bind remaining TMA to the polymer by formation of Al_2O_3 or $Al(OH)_x$. During TMA pulsing, a continuous increase in pressure is observed, reaching the maximum readout value of 2 mbar after 5 s. At a set bubbler temperature of 60 °C a maximum pressure of about 100 mbar could be reached, according to the vapor pressure of TMA.[25] For the high pressure reactor, described in detail elsewhere,[26] the process is comparable, but with higher base pressure. Similarly, the maximum readout value for the pressure of about 1 mbar is reached after 5 s of TMA pulsing. Saturation of remaining TMA residuals in the high pressure reactor is assumed to be reached due to water vapor in ambient air, which is used when venting the reactor for sample removal. In contrast to the low pressure reactor, the substrate holder in the high pressure reactor cannot be heated and all infiltration processes are conducted at room temperature (20 °C).

Influence of infiltration temperature on obtained mass gain during and after infiltration is captured via QCM (**Figure 1**). The PTMSP was spin coated on QCM gold crystals and a bare QCM crystal was used for reference. Infiltration was performed at 60 and 120 °C substrate temperature in the low pressure reactor. During infiltration, when TMA is present in the process atmosphere, a clear increase in mass gain can be seen for all infiltrated samples. This mass gain declines again when the TMA valve is closed and the reactor is evacuated. For the reference, one 60 s TMA pulse followed by a water pulse was monitored. During the first seconds when opening the TMA valve, a small increase in mass gain is observed, which declines over time although the TMA valve is still open. The initial increase is therefore likely attributed to an adaption of the system's frequency due to the sudden increase in pressure. A small net mass gain of about 150 ngcm^{-2} can be observed after introduction of the water pulse. This mass gain is assumed to correspond to one Al_2O_3 layer in addition to possible adsorption of water on the surface. In contrast, the infiltrated PTMSP samples show a net mass gain of 590 and 1524 ngcm^{-2} for temperatures of 60 and 120 °C, respectively. Exposing the samples to TMA for two more cycles without a water pulse in between showed no change in net mass gain. This net mass gain correlates to the amount of TMA trapped in PTMSP after evacuation of the reactor and subsequent desorption of unreacted TMA molecules. This means saturation and thus reaction with the functional group of the polymer is already reached after the first cycle. Further increase can only be seen when repeating the TMA cycles after introduction of the water pulse thereby creating fresh reaction sites. In this case, TMA is believed to then react with the Al_2O_3 nuclei formed by the water pulse. This would in consequence lead to stepwise growth of material inside the polymer resembling a conventional ALD process cycle. Due to the higher net mass gain and assumed higher infiltration degree for 120 °C all further infiltration processes in the low pressure reactor are performed at 120 °C unless noted otherwise.

The increase in net mass gain for elevated substrate temperature can be explained by the balance of diffusion and chemical reaction and their temperature dependency. As the glass transition temperature T_g of PTMSP is above 250 °C,[21] the polymer is in glassy state for both temperatures investigated. According to Padbury and Jur[27] an elevated temperature will increase the polymer's free volume thereby promoting diffusion of TMA into the bulk material. At the same time, the surface reaction rate with TMA increases at higher temperatures, inhibiting further precursor uptake. With regards to PTMSP, increasing the temperature will lead to a higher free volume and predominantly aid the diffusion of TMA into the polymer as seen by the higher mass gain for 120 °C compared to 60 °C.

2.2. Morphological Changes

Changes in surface morphology cannot be observed. AFM measurements show no significant differences in surface structures and the corresponding root mean square roughness (R_{RMS}) is similar for both untreated PTMSP and samples infiltrated in the low pressure reactor for 10 and 60 s, ranging from 1.77 to 1.92 nm (Figure S1, Supporting Information). This indicates that growth on the surface is likely to play a minor role compared to changes inside the polymer.

The contact angle of PTMSP changes after infiltration indicating a shift from hydrophobic to a more hydrophilic behaviour (**Figure 2**). Untreated PTMSP has a contact angle of 96.4°, which drops to 57.25° ± 1.77° and 54.9° ± 2.83° after 10 s and 2 x 20 s (no water pulse in between, as displayed in Figure 1) of

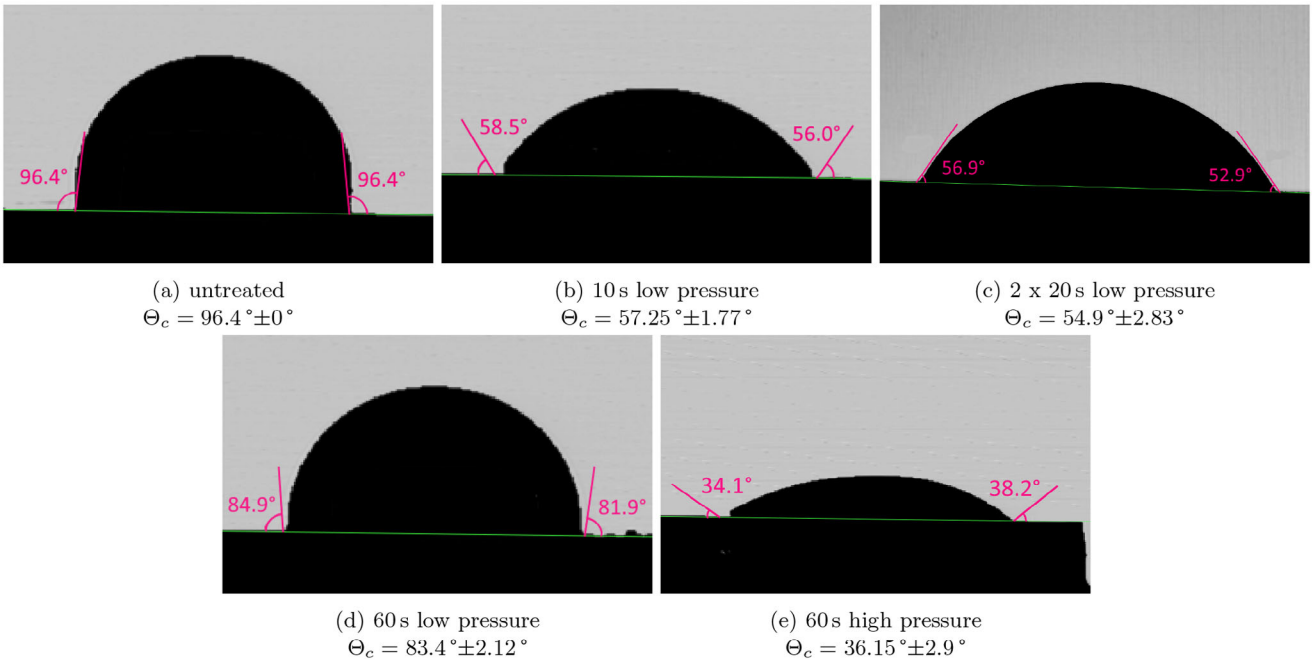

(a) untreated
$\Theta_c = 96.4\,^\circ \pm 0\,^\circ$

(b) 10 s low pressure
$\Theta_c = 57.25\,^\circ \pm 1.77\,^\circ$

(c) 2 x 20 s low pressure
$\Theta_c = 54.9\,^\circ \pm 2.83\,^\circ$

(d) 60 s low pressure
$\Theta_c = 83.4\,^\circ \pm 2.12\,^\circ$

(e) 60 s high pressure
$\Theta_c = 36.15\,^\circ \pm 2.9\,^\circ$

Figure 2. Contact angles Θ_c of PTMSP: a) untreated, b) 10 s low pressure, c) 2 × 20 s low pressure, d) 60 s low pressure, e) 60 s high pressure.

infiltration in the low pressure reactor, respectively. When infiltrated for 60 s in the high pressure reactor, the contact angle drops even lower to 36.15° ± 2.9°. An exception to this trend is the sample infiltrated for 60 s in the low pressure reactor, showing only a slightly lower contact angle of 83.4° ± 2.12°. As contact angle measurements are generally sensitive to surface conditions, results are only taken as a first indication, supporting the idea of successful infiltration and the overall effect being a shift toward more hydrophilic surfaces. A trend regarding infiltration time cannot be concluded with certainty. The initial contact angle of 96.4° for the hydrophobic PTMSP surface is close to literature values.[28,29] Infiltration with TMA and water induces the formation of aluminum-oxide or hydroxide moieties, as indicated by XPS measurements outlined in Section 2.3. This oxygen content arises from the reaction of chemisorbed species and TMA molecules remaining inside the polymer with water during the last step of the infiltration procedure. Both aluminum-oxide and hydroxide surfaces are known for their hydrophilic behavior,[30–33] which is reflected by the decreasing contact angle of the infiltrated samples. This trend is observed for all infiltrated samples, indicating successful aluminium incorporation. With regards to the sample infiltrated for 60 s in the high pressure reactor, the lower infiltration temperature of only 20 °C might additionally influence the obtained contact angle. Lower temperatures will result in slower diffusion of TMA into the polymer thus potentially aiding agglomeration of TMA close to the surface thereby impacting the measured contact angle.

Cross-section images taken via STEM reveal the different regions of PTMSP spin coated on SiO_2 with regards to chemical composition (Figure S2, Supporting Information). The regions can be divided as follows: i) carbon deposited to protect the sample during the focused ion beam (FIB) sample preparation ii) PTMSP polymer, iii) PTMSP-SiO_2 gradient layer, iv) SiO_2, and v) Si wafer substrate. As samples, untreated and infiltrated layers from both the low pressure and the high pressure reactor are investigated. Of special interest is the gradient layer between PTMSP and SiO_2 showing a gradient transition from inorganic substrate to organic polymer as seen more clearly from **Figure 3**. The origin of such a gradient layer is currently unknown to the authors, however. TEM images of gradient layer and SiO_2 substrate for these samples show morphological changes due to infiltration (**Figure 4**). While the untreated PTMSP appears porous, the size of these structures becomes smaller for the infiltrated samples. The smallest structures are observed for 60 s (high pressure). A clear correlation between infiltration time and structure size does not seem possible for the infiltration times investigated. In addition to the changes in the gradient layer region, structures of the SiO_2 substrate also seem to become finer when infiltrated. However, it should be noted that TEM images show only a fraction of the whole SiO_2 substrate and the oxide was not subject to detailed further investigations. It is therefore possible that the substrate in fact features a slightly different stoichiometry, e.g., induced by deposition of PTMSP, exhibiting lower density than native SiO_2 which in turn might allow for partial infiltration as visible in TEM images. Supporting this assumption, results from EDS measurements presented in the following show carbon concentrations between 1 and 5% in the SiO_2 region.

2.3. Infiltration Degree and Depth

Determination of aluminum concentration and infiltration degree is difficult due to an overall low aluminum content. XPS measurements of different infiltration processes varying infiltration time and temperature in the low pressure reactor show an

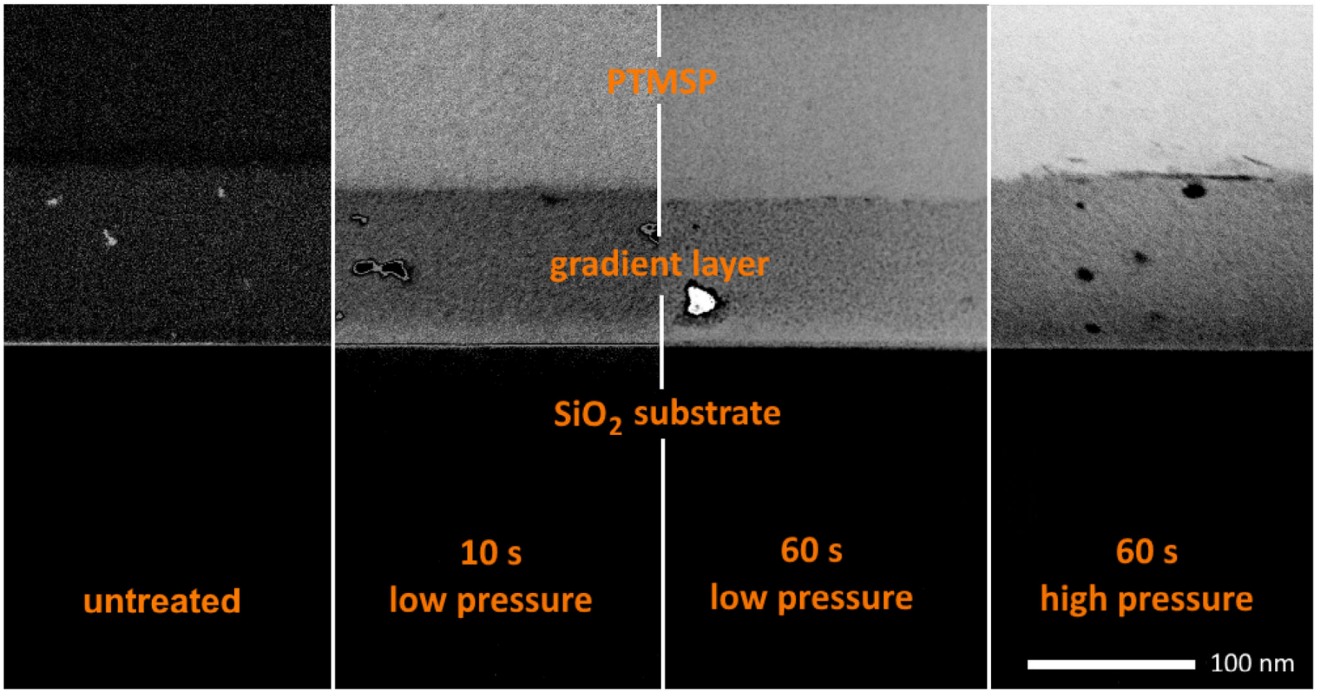

Figure 3. Cross-section of PTMSP spin coated Si wafers measured via STEM focusing the interface between gradient layer and SiO_2 substrate. The images have been modified in terms of contrast and color curves to highlight the gradient layer. The image for the 60 s low pressure sample was measured with a 50 nm scale, but has been resized accordingly.

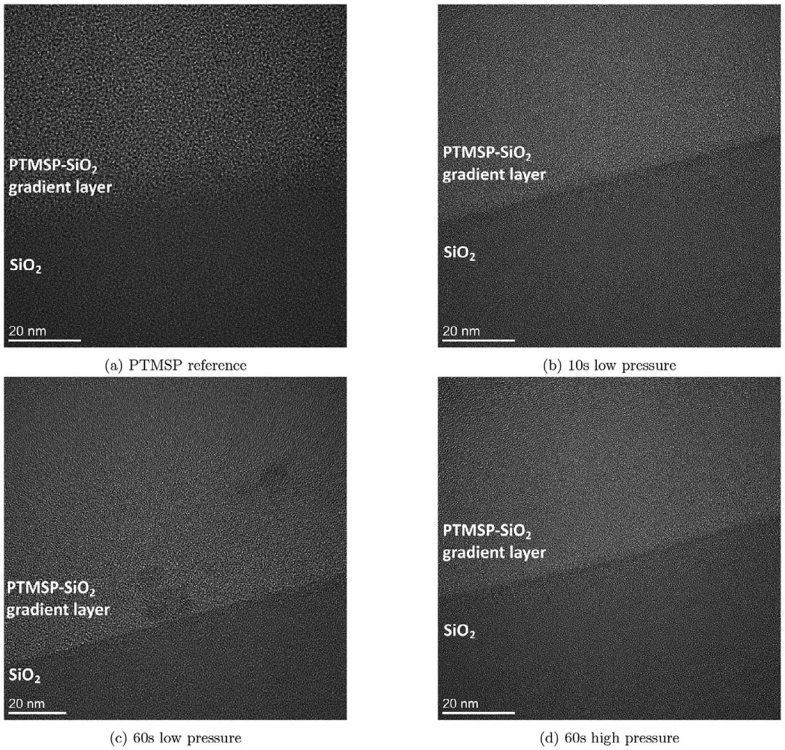

Figure 4. TEM cross-section images of PTMSP before and after infiltration. The cross-section shows the PTMSP-SiO_2 gradient layer and the SiO_2 substrate.

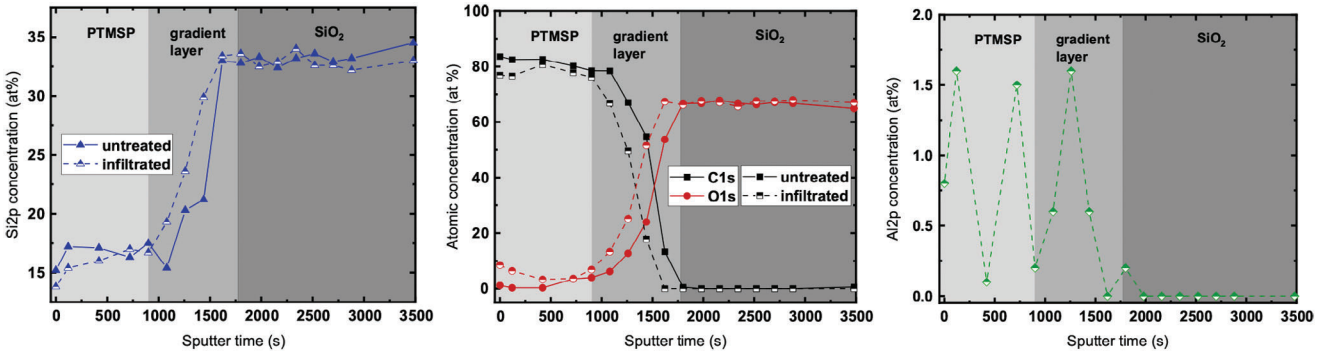

(a) Si2p (b) C1s and O1s (c) Al2p

Figure 5. Atomic concentrations of untreated and infiltrated (60 s low pressure) PTMSP sample as obtained from XPS measurements. The concentration profiles across the samples are shown for a) Si2p, b) C1s and O1s and c) Al2p. Al2p concentrations are only shown for the infiltrated sample as the untreated sample yielded no significant Al2p intensities.

average aluminum concentration of 1.8 ± 0.5 at.% close to the surface based on all infiltrated samples. The lowest concentration obtained is 1 at.% and the highest concentration 2.5 at.% (Table S1, Supporting Information). Due to the low concentration, errors are significant in these measurements and no clear trend can be obtained for variation of infiltration parameters such as temperature or time. In the high pressure reactor, variation of infiltration, and residence time (i.e., TMA valve closed, pumps still sealed off) leads to much higher aluminum concentrations measured close to the surface. A minimum aluminum concentration of 11 at.% and a maximum of 15.5 at.% is obtained (Table S1, Supporting Information). However, no clear trend is visible either and the lower infiltration temperature of 20 °C might lead to agglomeration at the surface due to lower diffusion. XPS depth-profiling of a sample infiltrated for 60 s in the low pressure reactor yields similarly low Al2p intensities (**Figure 5**). Aluminum concentrations according to the depth profile remain low and noisy with an average value of 0.9 ± 0.6 at.%. Due to these high errors, no significant trend was visible and peak-fitting for additional insight into the reaction mechanism is not feasible. Despite the low concentrations, infiltration is confirmed to have taken place as untreated PTMSP shows no aluminum signal. Additionally, the oxygen content measured in the PTMSP region increases for the infiltrated sample to an average of 4.8 ± 2.2 at.% compared to 0.3 ± 0.03 at.% for the untreated sample. This hints at possible formation of $Al(OH)_x$ or Al_2O_3 due to the water pulse after infiltration.

A more detailed insight into infiltration depth is obtained by TOF-SIMS. Intensity profiles of Si, Al, and AlO in dependence of sputter time for untreated and infiltrated PTMSP (60 s low pressure) are depicted in **Figure 6**. Al and AlO intensities differ greatly between untreated and infiltrated samples, with the intensities for infiltrated samples being significantly higher, further proving the successful infiltration. Al and AlO intensities feature two maxima, one close to the surface and one in the gradient layer region. Between these two maxima the profiles form a valley, with intensities dropping by a factor of 2 to 3. This could indicate aluminum agglomeration both at the surface and in the gradient layer. An increased Al and AlO signal can also be seen in the beginning of the SiO_2 substrate compared to untreated PTMSP. Considering the measurements were performed in positive polarity and oxygen was also used a background gas for charge compensation, the possibility of matrix effects has to be taken into account. Such a matrix effect might be responsible for the sharp increase of intensities at the surface which aligns with a similarly increased O signal (Figure S3, Supporting Information). Observation of a local maximum close to the surface is not

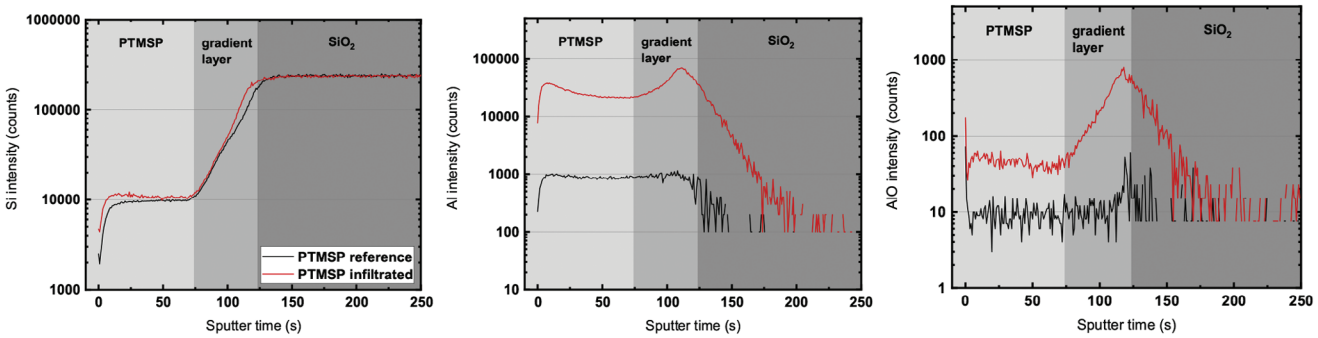

Figure 6. TOF-SIMS measurements of untreated PTMSP reference and infiltrated (60 s low pressure) PTMSP sample. The intensity profiles across the substrate are shown for the following elements: a) Si, b) Al, c) AlO.

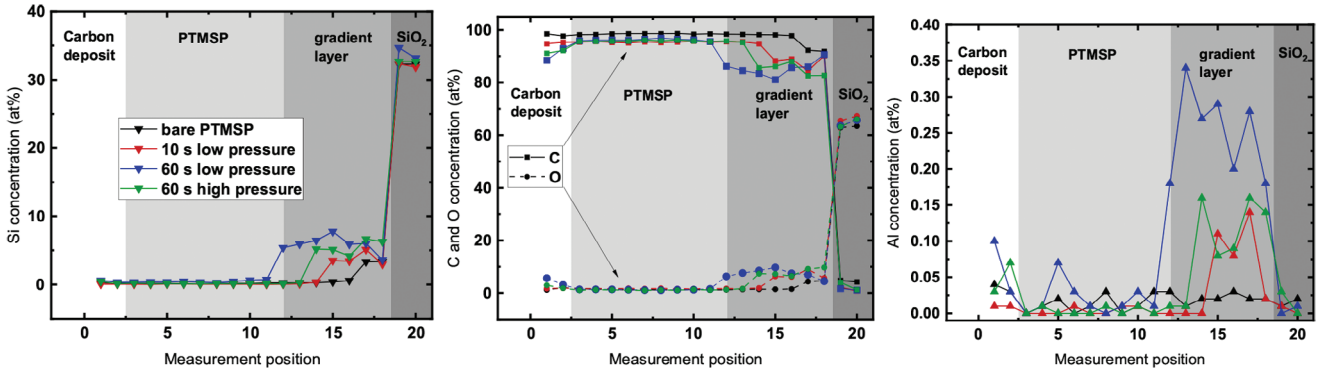

(a) Si concentration profiles (b) C and O concentration profiles (c) Al concentration profiles

Figure 7. Atomic concentration profiles of a) Si, b) C and O and c) Al as obtained from EDS measurements of cross-sections of infiltrated PTMSP samples. The cross-section covers the carbon deposition on the surface, the actual PTMSP, which is spin coated on a SiO_2 substrate, as well as the gradient layer between PTMSP and SiO_2/Si substrate. Lines serve as guide for the eye only.

uncommon with infiltration, however, as the monomer concentration is highest in this region increasing the chances for chemical reactions. This is in accordance with findings from Mai et al.,[24] who observed the same trend under several conditions. Except for the mentioned increase in the surface region, a significant influence of matrix effects is considered unlikely as the similarly influenced profile of Si correlates with XPS and EDS results and the presence of Al peaks at the gradient layer SiO_2 interface is observed in EDS profiles (see **Figures** 7 and 8) as well. The spike at the first measurement point for AlO is considered a measurement artifact and to lesser extent also seen for the untreated sample. The presence of Al and AlO signals also affecting the SiO_2 substrate could be the result of low resolution or knock-on effects. However, findings from TEM images (Figure 4) support this observation. Increased Al and AlO intensities in the gradient layer indicate favorable reaction sites being formed by a higher oxygen content in the gradient layer region. AlO intensities are low, however, and prone to measurement errors. One possible error could be the simultaneous sputtering of aluminum and oxygen, forming AlO only before entering the measurement device. Due to these low signal intensities, significance of AlO profiles is limited.

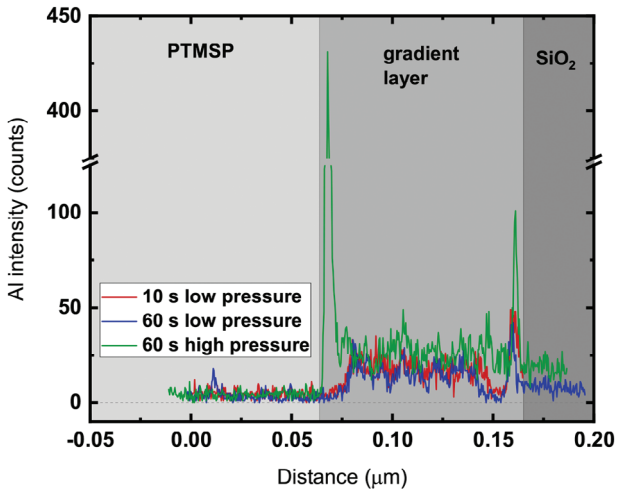

Figure 8. High resolution EDS measurement of aluminum intensity along the PTMSP-SiO_2 interface for samples infiltrated for 10 s (low pressure), 60 s (low pressure) and 60 s (high pressure).

Concentration profiles are obtained by EDS measurements. The samples measured are the same as for the STEM and TEM images and the results are displayed in Figure 7. Due to FIB sample preparation requiring deposition of a carbon top layer and PTMSP being a porous polymer with high free volume, the obtained concentration profiles do not reflect the real stoichiometry of PTMSP and carbon concentrations are overestimated. In the measured samples, carbon concentrations are above 95% reaching up to 98% for the untreated sample compared to a theoretical concentration of 86% according to PTMSP stoichiometry and as obtained from XPS measurements described earlier (see Figure 5). This effect is seen throughout the whole polymer reflecting its porous nature. At the same time, the increase in carbon concentration is impeded by infiltration as values drop from 98% for the untreated PTMSP to 95% for infiltrated samples confirming the earlier described findings of TEM images showing finer structures. This effect is also visible in the gradient layer region, showing increases of oxygen and silicon concentrations. These increases are stronger for infiltrated samples. Measured Al concentrations for the untreated sample are considered noise as neither XPS nor TOF-SIMS showed significant intensities for untreated PTMSP. Al concentrations in the PTMSP region are difficult to measure, as values are partially close to or below detection limit for the samples investigated. Al enrichment at the surface is indicated for both 60 s (low pressure) and 60 s (high pressure), correlating to observations from TOF-SIMS measurements (Figure 6). Al agglomeration in the gradient layer is seen for all infiltrated samples, also correlating well to TOF-SIMS measurements. High resolution measurements of the gradient layer region are performed to investigate this in more detail (Figure 8). In PTMSP, the Al intensity is low and rises when transitioning toward the gradient layer showing a distinct peak for 60 s (high pressure). In the gradient layer, Al intensity is increased in comparison to PTMSP as is also visible for both 10 s (low pressure) and 60 s (low pressure). A second distinct peak is

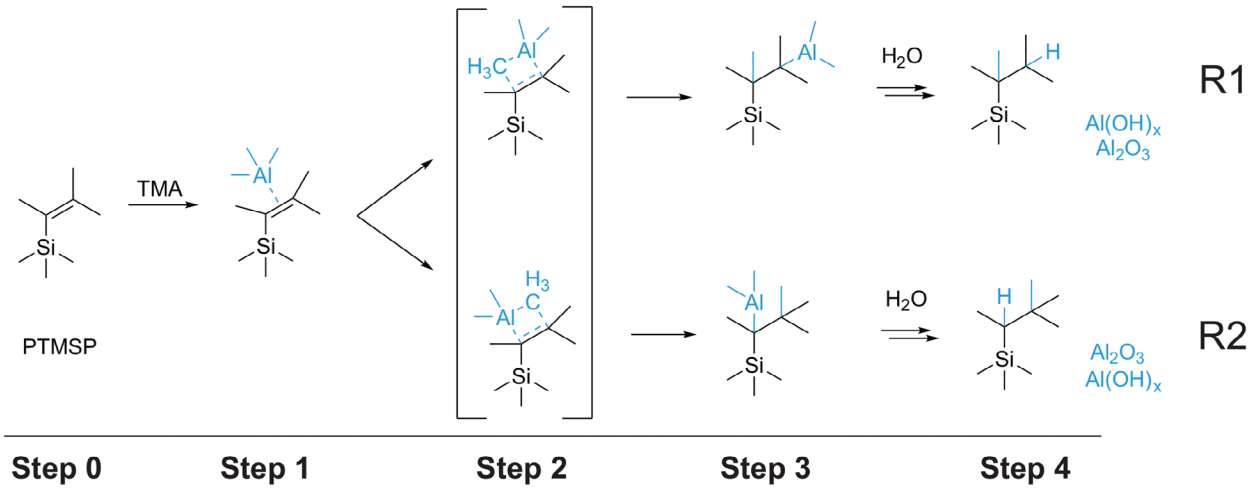

Figure 9. Chemical structure of poly(1-trimethylsilyl-1-propyne) (PTMSP) and possible reaction paths PTMSP undergoes when infiltrated with TMA.

present at the gradient layer to substrate interface, visible for all three infiltrated samples. Al intensity continues to be elevated in substrate region compared to PTMSP region, confirming results described earlier.

TMA seems to bind better to oxygen containing structures as is indicated by increased intensity in both gradient layer and SiO_2 substrate compared to organic PTMSP. Under consideration of the hard and soft acid and base concept (HSAB),[34,35] the higher TMA concentration in the gradient layer can be explained as follows: TMA is considered as a strong Lewis acid[36] and features ionic bonds between Al and its corresponding methyl groups, forming a hard Lewis acid-base pair. The carbon–carbon double bond in PTMSP is a covalent bond and acts as a soft Lewis base. In contrast, increased oxygen contents in the gradient layer lead to more likely formation of Si-O bonds or OH groups acting as hard Lewis bases. According to the HSAB concept, a hard Lewis acid such as Al is therefore more likely to react with a hard base, in this case the oxygen rich gradient layer. Taking this into account, it is assumed for the gradient layer that reactions of TMA with oxygen are preferred over reactions with the carbon–carbon double bond. In addition, accumulation of Al in the gradient layer can be attributed to the fact that TMA can easily penetrate the porous polymer, while the diffusion will be slowed in the gradient layer due to the higher density of this material. Increased reaction times therefore allows more TMA to bind to the gradient layer or SiO_2. At the same time, the presence of oxygen in the gradient layer under consideration of the HSAB concept should lead to a higher reactivity inducing stronger densification of the material as seen in Figure 4. In this context, the formation of peaks at the interface of gradient layer and SiO_2 can attributed to gradual densification and increase in oxygen content toward the SiO_2 substrate. The dependence on spatial distribution in VPI processes on diffusion and reaction rates is also described in detail by Ren et al.[37] The existence of the second peak at the PTMSP-gradient layer interface seen for the sample infiltrated for 60 s in the high pressure reactor cannot be explained with certainty as neither the other samples nor TOF-SIMS show this second peak. These differences are therefore believed to stem from the difference between the low and high pressure reactor, e.g., reactor volume, base pressure or application of water pulse for entrapment of TMA.

2.4. Theoretical Description and Correlation to Experiments

PTMSP contains a reactive carbon-carbon double bond that can react with TMA. The reaction is believed to be triggered by the electron deficiency of TMA in combination with the electron-rich double bond. The proposed reaction pathways (depicted in **Figure 9**) follow similar reactions known as hydroboration in the organic chemistry and specifically methylation reactions via TMA as described by Pasynkiewicz.[38] Specifically, the reaction of TMA with alkynes and alkenes is documented for carboalumination reactions. In literature, examples are Zr-catalyzed asymmetric carboalumination of alkenes and Zr-catalyzed carboalumination of alkynes, respectively.[39,40] TMA can attach to both sides of the carbon–carbon double bond resulting in the two possible reaction paths. After initial docking to the double bond, one methyl group is added to one side of the double bond with the remaining dimethylaluminum binding to the other side. When introducing the water pulse, formation of either $Al(OH)_x$ or Al_2O_3 is expected. DFT simulations have been conducted for calculation of reaction energies required. Based on the energy differences between reaction path R1 and R2, insights on the more probable reaction are possible. In the third reaction step, when TMA has eliminated the carbon-carbon double bond to attach to one of its sides, the energy difference $\Delta E_{R1\text{-}R2}$ is 0.818 eV. Al is therefore more likely to attach to the outer side of the former carbon–carbon double bond, while the methyl group will likely bind in closer proximity to the methyl groups attached to the silicon atom. After introduction of the water pulse in reaction step 4, this energy difference declines significantly, yielding $\Delta E_{R1\text{-}R2}$ = -0.049 eV. Formation of Al_2O_3 or $Al(OH)_x$ groups is therefore likely in both proposed positions and no preference can be determined.

IR difference spectra (i.e., the untreated PTMSP spectrum has been subtracted from the infiltrated spectra) are portrayed in **Figure 10** for both experimental and simulated data. For the

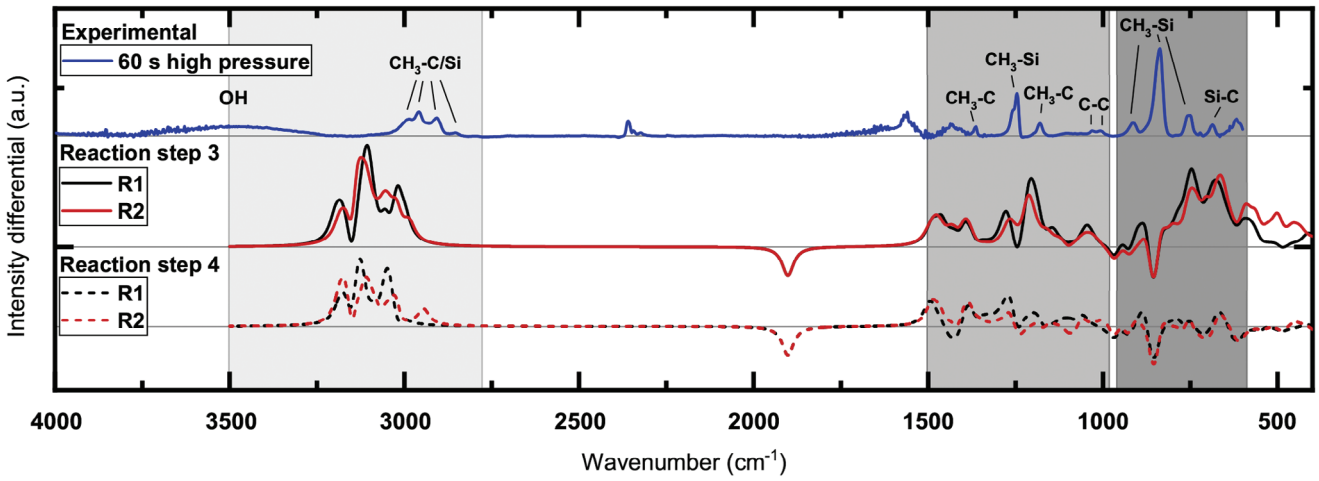

Figure 10. Comparison of changes in IR spectrum from experiment and simulation after infiltration of PTMSP with TMA. Regions of interest are highlighted. For the experimental results, the measured IR spectrum of untreated PTMSP was subtracted, for the simulated spectra R1 and R2, the simulated spectrum of PTMSP was subtracted. Experimental data was subject to baseline correction and normalized with respect to Si-O-Si at 1110 cm^{-1} originating from the underlying SiO_2 substrate. For the experimental spectra, bonds have been assigned to their respective peaks based on literature values.[41]

experimental spectra, impact of infiltration in the high pressure reactor was generally visible best, hence difference spectra of these samples are used. Difference spectra of samples infiltrated in the low pressure reactor, however, show good resemblance to those of the high pressure reactor and are thus assumed to follow the same reaction path (Figure S6, Supporting Information). References for correlation of observed changes to either PTMSP or alumina related peaks can be found in literature.[41–44] Such bonds are assigned to their respective peaks in Figure 10. Considering the reaction path outlined in Figure 9, the following changes in the IR spectrum would be expected:

1. loss of C=C bond: decrease in 1548 cm^{-1} intensity
2. formation of C-C instead of C=C bond: increase in 1010 cm^{-1} and 1025 cm^{-1} intensities
3. addition of methyl group from TMA to newly formed C-C bond: increase in 1178, 2852, and 2984 cm^{-1} intensities
4. addition of Al at newly formed C-C bond and formation of $Al_2O_3/Al(OH)_x$ groups in free volume after water pulse: increasing intensity at 630, 760, 900, and 958 cm^{-1}
5. formation of OH after water pulse: 3370 and 3500 cm^{-1}

In the experimental spectra OH formation is visible, showing a broad band ranging from 3750 to 3200 cm^{-1}. Addition of methyl groups is seen in multiple peaks across the measured spectra. Increasing intensities are observed at 2987, 2852, 1363, and 1180 cm^{-1}. The increase in intensities at 1030 and 1007 cm^{-1} is small compared to other changes, but might indicate formation of C-C instead of C=C. However, a decrease in intensity at 1548 cm^{-1} correlating to a loss of C=C bonds cannot be observed. Instead, experimental data shows an increase for this wavelength, but this is assumed to rather stem from atmospheric influences, not sufficiently compensated in post-processing of the data. As pointed out by Svatoš and Attygalle,[45] internal carbon–carbon double bonds are unlikely to show in IR spectra due to little impact of stretching on dipole moments. Aluminum related bonds (e.g., Al_2O_3 or $Al(OH)_x$) cannot be clearly assigned. These either do not match in wavenumbers or overlap with CH_3-Si bonds of PTMSP as is the case for 760 cm^{-1}. Further changes in the experimental spectra can be assigned to CH_3-Si and Si-C bonds, which are possibly impacted by the infiltration induced changes to PTMSP, affecting e.g., structure or orientation.

Simulated difference spectra displayed in Figure 10 are used to confirm whether the observed changes in the experimental data are due to infiltration or caused by other effects such as possible contamination of samples or atmosphere. Simulations have been conducted for a single untreated PTMSP molecule as well as the single molecules depicted in steps 3 and 4 of the reaction mechanism (Figure 9). Both pathways have been simulated. Additional byproducts are not included in the simulated spectra. For the simulated difference spectra, the simulated PTMSP spectrum has been subtracted from the simulated spectra of reaction steps 3 and 4. Due to simplifications in the modelling, simulated IR spectra are known to deviate in their wavenumbers. Often this leads to an overestimation of wavenumbers.[46] This can be corrected using frequency scaling factors.[46] For the simulated spectra calculated in the frame of this work, no correction was performed and the spectra are only compared in their qualitative trends. The most prominent differences in the simulated spectra can be found in the ranges of 3500 – 2800 cm^{-1}, 1500 – 1000 cm^{-1} and 950 – 600 cm^{-1}, highlighted in Figure 10. OH formation is not observed in the simulated spectra as no byproducts formed by the water pulse were included in the simulation. Addition of methyl groups in the range from 3250 to 2800 cm^{-1} is visible for all simulated spectra and correlates well to the changes observed experimentally. A clear deviation in wavenumbers is evident, however. Assigning simulated peaks in the remaining spectrum directly to corresponding bonds of PTMSP or the reaction mechanism is not possible due to this deviation in wavenumbers. The qualitative trend observed in the ranges 1500 – 1000 cm^{-1} and 950 – 600 cm^{-1} still shows similarities between experimental spectra and simulated spectra from reaction step 3. Relative intensities from reaction step 4 are significantly lower and most

prominent in the 3500 – 2800 cm^{-1} region. The shape of the spectrum from reaction step 4 in this region correlates well with that of the experimental data. Differences between the two reaction paths R1 and R2 are small hence no statement regarding the likeliness of one path can be made. In the simulated spectrum of untreated PTMSP (see Figure S7, Supporting Information) no peak correlating to C=C is visible thereby confirming the assumption of atmospheric influence in the experimental spectra for the related peak. Moreover, the lack of Al related bonds in the spectra is supported by the simulation by comparing spectra of simulated Al_2O_3 and $Al(OH)_3$ molecules to untreated PTMSP and reaction steps 3 and 4 (Figure S7, Supporting Information).

2.5. Permeation

Measurements using cyclic voltammetry (CV) are used to further investigate changes in the porous structure of the PTMSP samples. For this purpose, silicon wafers are sputtered with gold before application of the PTMSP polymer to allow for electron exchange when using the gold surface as the working electode (see Section 4 for more details). All measurements including the PTMSP reference lack clear redox peaks in their respective voltammogram (see Figure S5, Supporting Information). According to Hoppe et al.[47] this indicates either pore sizes smaller than 0.95 nm (defined by the size of ferrocyanide in the electrolyte solution) or a very small number of pores relative to the measured area. This argument is in accordance to the earlier described TEM measurements showing a densification of the porous structure. Interestingly, the lack of redox peaks is already visible for the untreated PTMSP reference. As the untreated PTMSP sample was not freshly rejuvenated immediately before measurement, it can be assumed it had already undergone aging. As aging reduces the free volume of PTMSP, this will subsequently lead to a reduction in permeability.[22,48] Thus, aging induced reduction in free volume is likely to inhibit the transport of ferrocyanide as observed in the voltammogram. In addition, the generally reduced current with stronger infiltration is an indicator for the dependence of PTMSP permeability on the infiltration process.

This dependence is also seen when analyzing the gas permeance, commonly measured in units of GPU (gas permeation units). The results are displayed in **Figure 11**. For these measurements, 70 nm thick PTMSP is coated on porous PAN support membranes and then infiltrated. Two independent measurement series are conducted: i) parameter screening using wider step sizes (0.1, 1, 10, and 60 s) and ii) investigation of area of interest using smaller step sizes (0.2, 0.4, 0.6, 0.8, 5, and 10 s). The first measurement series (Figure 11) shows only a small decline for 0.1 s of infiltration compared to untreated samples with permeances being above 1000 GPU for all gases measured. This decline is increasing for longer infiltration times with permeance values eventually falling below the measurement device's detection limit and partially showing no measurement signal for 60 s infiltration time. The second measurement series first shows a slight increase in permeance from 0.2 to 0.4 s. This is followed by a decrease, again becoming stronger with prolonged infiltration time. At 10 s infiltration time for

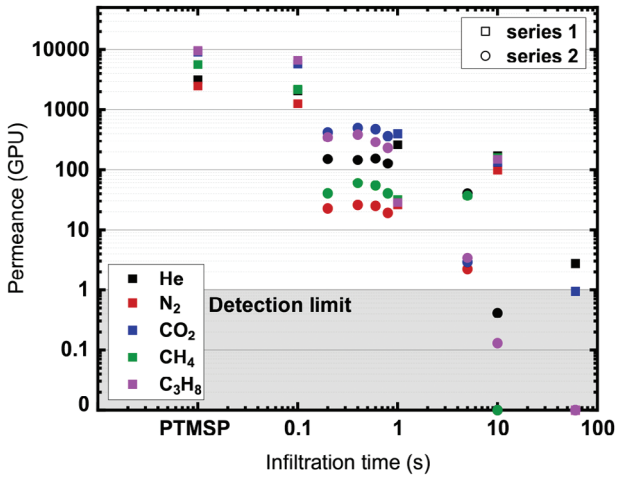

Figure 11. Permeance (gas permeation units - GPU) in dependence of infiltration time for helium (He), nitrogen (N_2), carbon dioxide (CO_2), methane (CH_4) and propane (C_3H_8). Two independent series of measurements were performed (series 1, series 2). Measurements showing 0 GPU correspond to no signal detected. Moreover, measured permeation values below 1 GPU are below the device's detection limit thereby limiting their significance.

this measurement series, all measured signals are below detection limit. This is in contrast to the first measurement series at 10 s infiltration time, for which obtained permeation values differ clearly from those of the second measurement series and moreover lack the selectivity of all other measured samples as explained in the following. It is assumed that small defects in the polymer could be the cause as these would induce both an increase in permeation and the loss of selectivity. With regards to selectivity, a growing spread between the gases' permeance values can be seen when comparing the untreated sample to infiltrated samples. For the untreated sample, permeance values range from 2506 GPU (N_2) to 9618 GPU (C_3H_8), a factor of 3.84 in difference. This factor between C_3H_8 and N_2 increases to 5.24 for 0.1 s infiltration time and rises to its maximum of 15.3 for 0.2 s infiltration time. The overall changes to the permeation behaviour can be explained as follows: Up to 1 s of infiltration time, samples feature solubility dominated transport as gases such as CO_2 and C_3H_8 with high solubility permeate fastest. This is identical to the transport behavior typical for PTMSP. For infiltration times of 1 s and longer, the role of diffusion based transport becomes more important. The decrease in free volume limits diffusion and has stronger impact on molecules with bigger kinetic diameter. This is specifically visible when comparing permeance values of a large molecule such as C_3H_8 to the small He molecule. He permeance is affected the least by the decreasing free volume from infiltration whereas C_3H_8 permeance declines significantly stronger. The high solubility of C_3H_8 can therefore no longer compensate the slower diffusion due to decreased free volume. In terms of significance of the obtained permeance/selectivity values, the CO_2/N_2 selectivity of 19.2 for 0.4 s infiltration time and a CO_2 permeance of 495 GPU are comparable to the results by Pramanik and Regen,[23] who modified PTMSP via thiol-ene click reactions.

3. Conclusion

A new VPI process of TMA into PTMSP was developed and its effects on the polymer as well as the implication with regards to its permeation behavior were investigated. Based on the results from QCM and the documented changes to structure and depth dependent stoichiometry, it can be concluded that VPI using TMA into PTMSP is possible. The presence of Al along the whole polymer was detected, which confirms that the VPI process affects the whole polymer and is not limited to the sub-surface or the gradient layer region. A significant densification of the porous structure was observed. The measured permeance values of the PTMSP membranes show a decline with prolonged infiltration time. In this sense, the densification of the material seems to be directly correlated to the strong decrease in permeance for longer infiltration times, falling even below the device's detection limit. For shorter infiltration times, however, selectivity of for instance CO_2/N_2 improves, indicating possible applications in the membrane sector. Overall, permeation results in dependence on the infiltration time outline the versatility of the technique, being able to both aid membrane related applications or blocking gas permeation totally, depending on the desired application.

The reaction mechanism proposed in this work was investigated using IR analysis and DFT energy calculations. Observed changes in the IR spectra overall aligned well with expected changes suggesting that a reaction of TMA with a polymer featuring a carbon–carbon double bond functional group is possible. The increased Al formation in oxygen-enriched surroundings suggests a lower reactivity of the carbon–carbon double bond in comparison to oxygen containing bonds. This reaction mechanism represents just one possibility, however. Investigation of the significance of the carbon–carbon double bond or alternative reactions mechanisms requires in situ analysis and could be of interest for future studies.

Based on the strong influence of oxygen containing bonds within the polymer and its impact on reactivity with TMA, additional methods of facilitating VPI into PTMSP or possibly other polymers could be of interest. One of such methods is an additional pre-treatment step of the polymer with an oxygen plasma to oxidize the polymer and allow for enhanced TMA reactions. Depending on the specific plasma, various optimizations of the process could become feasible. Also, with regard to the high bandwidth of permeability achievable via VPI, more research into using it for more effective gas barrier layers is proposed.

4. Experimental Section

PTMSP Preparation and Rejuvenation: Synthesis of the PTMSP solution followed the procedure described by Rubner et al.[22] The solution contains 1.35 wt.% PTMSP (128.29 gmol^{-1}, abcr GmbH) dissolved in toluene (purity > 99.9%, VWR International S.A.S.) and was stirred for a minimum time of 24 h. After filtration using PTFE syringe filters (1 µm), the solution was spin coated on silicon wafers with a 500 nm thick oxide surface layer. After coating, the samples were dried at ambient air for at least 12 h. Ellipsometry was used to estimate the thickness of the obtained PTMSP coatings, as described elsewhere.[49] For the given procedure, all samples had an estimated thickness of about 90 nm.

For the PTMSP membranes, a polyacrylonitrile (PAN) composite membrane acts as the substrate for the PTMSP layer and was supplied by the Helmholtz-Zentrum Hereon Geesthacht. It consisted of a non-woven fabric and a microporous support structure of PAN. PTMSP was applied by dipcoating the substrate membrane in a bath containing the earlier mentioned PTMSP/toluene solution leading to about 70 nm thin PTMSP layers. Therefore, pieces of 4 x 4 cm were fixed on glass slides using tape around the edges of the membrane to avoid PTMSP coating on the nonwoven fabric. Afterward, the samples were dried at ambient air for at least 12 h.

To ensure a defined state of the polymer, every sample was rejuvenated directly before infiltration. For this purpose, the sample was submerged in methanol for 10 min, which would lead to swelling thereby reinstating the original high free volume state of PTMSP.[22] Afterwards, the methanol was evaporated by placing the sample on a heating plate (160 °C) for further 10 min. Alternatively, the remaining methanol could also be evaporated under vacuum conditions using lower temperatures. For all experiments involving the low pressure setup, evaporation of methanol was conducted under vacuum at 120 °C. Rejuvenation and infiltration using PTMSP membrane sheets were conducted at a lower temperature of 90 °C to prevent damage to the porous support membrane.

Experimental Diagnostics—Quartz Crystal Microbalance: In situ QCM experiments were conducted using gold coated AT-cut quartz crystals (f_{res} = 6 MHz). The crystal-holder was custom-built and connected to a SO-100 Oscillator and a SQM-160 thin film deposition monitor (JCM, Inficon).

Atomic Force Microscopy: AFM measurements of selected samples were conducted using a JPK NanoWizard 3 (Bruker Optics) device in the tapping mode at a frequency of 218 kHz, a line rate of 1 Hz and a scan resolution of 512 x 512 pixels. Recorded images were processed with JPK Data Processing software by subtracting a polynomial fit from each scan line and, wherever necessary, replacement of outliers. The processed images were further analyzed using the the open-source software Gwyddion.[50]

Contact Angle Measurements: Water contact angle measurements were conducted with a Phoenix 150 system (SEO) equipped with a XC-ST50 CCD camera (Sony) and Zoom 7000 macro video lens (Navitar). Prior to measurements, samples were cleaned with an Argon gas stream. Due to the device's camera providing only low resolution, images had been increased in their contrast by converting droplet colors to black to aid evaluation. Contact angles had been estimated using the open-source software OpenDrop.[51]

Fourier-Transformed Infrared Spectroscopy: Polymer characterization via FTIR spectroscopy was conducted using a Bruker Vertex 70 (Bruker Optics) with attached Hyperion 3000 microscope system. Each obtained spectrum was derived from 32 scans, featuring a spectral resolution of 2 cm^{-1}. All samples were measured in transmission mode on oxidized silicon wafers and were subject to atmospheric compensation due to ambient air conditions. Reference measurements were performed without any substrate, i.e., in air. For comparison purposes, all spectra were baseline corrected and normalized with respect to the peak at 1110 cm^{-1} originating from the underlying SiO_2 substrate.

Time of Flight Secondary Ion Emission Mass Spectroscopy: Depth-profiles using TOF-SIMS were obtained with a TOF.SIMS 5 system (IONTOF) operating in the "dual beam depth profiling" mode. As sputter beam, Xe ions were used at 1 keV ion energy. The sputter area was chosen to 400 × 400 µm^2. For the analysis, a Bi_3^+ ion beam was used at ion energies of 30 keV. The area analyzed was set to 100 × 100 µm^2. The measurements were performed in positive polarity. Charge compensation was achieved using O_2 as a background gas. The pressure was set to $4 \cdot 10^{-3}$ Pa.

X-ray Photoelectron Spectroscopy: XPS spectra were recorded using two different devices. Spectra acquired close to the polymer surface for proof of infiltration were measured using a Phi 5000 Versaprobe system (ULVAC-Phi Inc.) equipped with a Al Kα source. The take-off angle was set to 45° and the spot size to 100 µm. XPS depth-profiling was conducted using a Versaprobe II (ULVAC-Phi Inc.) instrument. It features a monochromatic Al Kα source and had an Argon ion source equipped for sputtering. The sputter voltage was set to 1 kV for a target emission current of 7 mA. The sputter crater was 3 × 3 mm^2 and the take-off angle 45°. Samples were sputtered with Ar ions for up to 3480 s. Atomic concentrations were calculated using the Unifit software by integration of the corresponding peak areas after baseline correction and by multiplication with the corresponding normalization factors.

(Scanning) Transmission Electron Microscopy, Energy-Dispersive X-ray Spectroscopy: STEM, TEM and EDS measurements were recorded using a JEM-ARM200F NEOARM (JEOL) aberration probe corrected TEM. The acceleration voltage was set to 200 kV for all measurements. Cross-sections of the samples were prepared with a dual-beam FEI Helios G4 CX (Thermo Fisher Scientific) FIB system. Protection from the ion beam was ensured by prior deposition of a carbon film on the samples. Carbon deposition, ion milling, and lifting out of the samples were carried out using a 30 kV ion beam. Final processing of the samples, i.e., lamella thinning, involved application of first, a 16 kV and following, a 8 kV ion beam.

Ellipsometry: Ellipsometric investigation for determination of PTMSP thickness was carried out using an RC2 ellipsometer (J.A. Woollam Co. Inc.) with a spot size of 2 mm. Measurements employ incident angles of 65°, 70° and 75° covering wavelengths from 192–1000 nm with a spectral resolution of 2 nm. The procedure of the ellipsometric modelling and subsequent thickness determination was the same as described by Rubner et al.[22] In a first step, the thickness of the oxide layer was determined using literaturevalues.[52] The PTMSP layer was modelled using a Cauchy parametrization ($n(\lambda) = A + B/\lambda^2$). The gradient layer between PTMSP and SiO_2 was not included in the modelling. The authors assumed this to be one of the reasons why calculated thicknesses via Ellipsometry deviate from thicknesses observed in cross-sections by STEM.

The refractive index was determined for a wavelength of 632.8 nm. Details on the ellipsometric modelling and the subsequent thickness determination were provided by Rubner et al.[22]

Cyclic Voltammetry: CV measurements were conducted with a PalmSens4 (PalmSens BV) potentiostat. The voltage was varied from -0.1 to 0.5 V, featuring a scan rate of 0.1 Vs^{-1}, a step size of 0.01 V and an equilibration time of 1 s. The measurements were carried out on conductive gold sputtered silicon wafers on which deposition of PTMSP and subsequent VPI was performed as described before. The gold sputtered silicon acts as the working electrode, a saturated calomel reference and a platinum counter electrode are placed 10 mm above the working electrode. As the redox active electrolyte solution, an aqueous solution of 10 mM ferrocyanide ($K_4[Fe(CN)_6]$) was chosen. Each sample was measured at least twice with four measurement cycles being recorded per measurement to account for reproducibility and the time needed to reach steady-state conditions. Further information on the CV measurements and analysis could be found elsewhere.[53,54]

Permeability: A constant volume variable pressure approach was used for the membrane permeability measurements. Details on this method were described by Koester et al.[55] Better accuracy for the obtained permeation results was achieved by performing and averaging six permeation measurements for each gas per membrane sample. The gas purities employed for the measurements were helium 5.0, nitrogen 5.0, carbon dioxide 4.5, methane 4.5 and propane 2.5. Measurements conducted use the gases in the order specified. The temperature of the heating cabinet and resulting feed stream was 24 ± 2 °C. The applied feed pressure was set to 1.5 bar.

DFT Calculations—Geometry Optimization and Energy Calculation: Energy calculations and simulation of infrared spectra were conducted using the same methods and tools as described by Mai et al.[24] Geometry optimization of the PTMSP polymer and its reaction products when infiltrated with TMA was performed using the Quickstep module[56] implemented in cp2k.[57] The underlying method was the Gaussian and plane waves method (GPW). Infrared intensities were calculated using Grimme's dispersion correction D3[58,59] with the Perdew-Burke-Ernzerhof (PBE) exchange-correlation functional.[60] In addition, a double-zeta basis set (DZVP-MOLOPT-SR-GTH)[61] was employed in combination with the corresponding Goedecker-Teter-Hutter (GTH) pseudopotentials.[62] The obtained IR intensities were subject to a 16 Å cutoff. The open-source tool Avogadro[63] was used for modeling of the isolated polymer, TMA, Al_2O_3 and $Al(OH)_x$. Using the calculated potential energies of the products, the potential energy differences of the analyzed reaction paths were obtained by subtracting the product energies (reaction pathways R1 and R2) from the educt energies (TMA + PTMSP).

Computational Vibrational Analysis: The vibrational analysis also follows the procedure provided by Mai et al.[24] The software Molden was used to obtain the IR spectra, which were estimated by applying a Lorentzian distribution to the intensities of the normal modes. These IR intensities were calculated as the derivative of the dipole along the normal modes in a static calculation. The obtained spectra were not adjusted in their frequencies and were therefore only used for comparison of qualitative trends. Matching of simulated wave numbers to experimental data was possible using frequency scaling factors as described in detail by Merrick et al.[46] Detailed information on various methods for calculation of vibrational spectra from ab initio molecular dynamics could be found in a study by Thomas et al.[64]

Statistical Analysis: Data within the text was displayed as mean ± standard deviation (SD).

Supporting Information

Supporting Information is available from the Wiley Online Library or from the author.

Acknowledgements

The authors are grateful for the support and funding provided by the German Research Foundation (DFG) within the frame of the Transregional Colloborative Research Center SFB-TR 87. A.D., T.d.l.A. and T.K. acknowledged the funding from the DFG INTRAPOL project 519869949. Support by the Interdisciplinary Center for Analytics on the Nanoscale (ICAN) of the University of Duisburg-Essen (DFG RIsources reference: RI_00313), a DFG-funded core facility (Project Nos. 233512597 and 324659309), is gratefully acknowledged. The authors are thankful for the support in XPS measurements from Ulrich Hagemann from ICAN. The authors would like to acknowledge the Jülich Supercomputing Centre (JSC) for computing time on the GCS Supercomputer JUWELS and the Paderborn Center for Parallel Computing (JC2) for computing time on the FPGA-based supercomputer NOCTUA. Open Access funding enabled and organized by Projekt DEAL.

Conflict of Interest

The authors declare no conflict of interest.

Author Contributions

Conceptualization is performed by A.D., N.B., J.J., F.Z., and J.R. Methodology is performed by N.B., F.Z., and J.J. Software is developed by F.Z. Validation is provided by J.J. Formal analysis is performed by J.J, N.B., F.Z., F.P., T.d.l.A., J.R., and J.F. Investigation is done by J.J., N.B., A.K., F.P., F.Z., J.R., V.R.D., and J.F. Resources are provided by A.D., P.A., J.R., T.K., M.W., and R.D. Data curation is performed by J.J., N.B., V.R.D., T.d.l.A., A.K., and J.R. Writing - original draft is written by J.J. Writing - review and editing is done by J.J., F.Z., N.B., T.d.l.A., F.P., J.R., A.D., P.A., J.F., V.R.D., A.K., T.K., M.W., and R.D. Visualization is performed by J.J. Supervision is done by A.D., J.J., N.B., P.A., T.K., M.W., and R.D. Project administration is done by A.D., P.A., T.K., M.W., and R.D. Funding acquisition is provided by A.D., P.A., T.K., M.W., and R.D.

Data Availability Statement

The data that support the findings of this study are available from the corresponding author upon reasonable request.

Keywords

gas separation, membrane, PTMSP, TMA, vapor phase infiltration

Received: February 23, 2024
Revised: July 3, 2024
Published online: August 13, 2024

[1] A. Zamboulis, N. Moitra, J. J. E. Moreau, X. Cattoën, M. W. C. Man, *J. Mater. Chem.* **2010**, *20*, 9322.
[2] S. Nasreen, M. L. Baczkowski, G. M. Treich, M. Tefferi, C. Anastasia, R. Ramprasad, Y. Cao, G. A. Sotzing, *Macromol. Rapid Commun.* **2018**, *40*, 1800679.
[3] Z. Chen, H. Wang, X. Wang, P. Chen, Y. Liu, H. Zhao, Y. Zhao, Y. Duan, *Sci. Rep.* **2017**, *7*, 40061.
[4] V. S. V. Satyanarayana, V. Singh, V. Kalyani, C. P. Pradeep, S. Sharma, S. Ghosh, K. E. Gonsalves, *RSC Adv.* **2014**, *4*, 59817.
[5] J. T. Diulus, R. T. Frederick, D. C. Hutchison, I. Lyubinetsky, R. Addou, M. Nyman, G. S. Herman, *ACS Appl. Nano Mater.* **2020**, *3*, 2266.
[6] A. K. T. Taha, M. Amir, A. D. Korkmaz, M. A. Al-Messiere, A. Baykal, S. Karakuş, A. Kilislioglu, *J. Inorg. Organomet. Polym. Mater.* **2018**, *29*, 979.
[7] Y. Bautista, M. Gómez, C. Ribes, V. Sanz, *Prog. Org. Coat.* **2011**, *70*, 358.
[8] S. Pandey, S. B. Mishra, *J. Sol-Gel Sci. Technol.* **2011**, *59*, 73.
[9] S. M. George, *Chem. Rev.* **2009**, *110*, 111.
[10] P. Sundberg, M. Karppinen, *Beilstein J. Nanotechnol.* **2014**, *5*, 1104.
[11] H. B. Profijt, S. E. Potts, M. C. M. van de Sanden, W. M. M. Kessels, *J. Vac. Sci. Technol. A: Vac. Surf. Films* **2011**, *29*, 050801.
[12] A. Subramanian, N. Tiwale, C.-Y. Nam, *JOM* **2018**, *71*, 185.
[13] R. R. Petit, J. Li, B. V. de Voorde, S. V. Vlierberghe, P. F. Smet, C. Detavernier, *ACS Appl. Mater. Interfaces* **2021**, *13*, 46151.
[14] W. Kafrouni, V. Rouessac, A. Julbe, J. Durand, *J. Membr. Sci.* **2009**, *329*, 130.
[15] J. Rubner, S. Skribbe, H. Roth, L. Kleines, R. Dahlmann, M. Wessling, *Membranes* **2022**, *12*, 994.
[16] S. Yi, B. Ghanem, Y. Liu, I. Pinnau, W. J. Koros, *Sci. Adv.* **2019**, *5*, eaaw5459.
[17] N. Ahmad, C. Leo, A. Ahmad, M. N. Izwanne, *Sep. Purif. Technol.* **2019**, *212*, 941.
[18] E. K. McGuinness, F. Zhang, Y. Ma, R. P. Lively, M. D. Losego, *Chem. Mater.* **2019**, *31*, 5509.
[19] R. W. Baker, *Membrane technology and applications*, 3rd ed edition, Wiley-Blackwell, Oxford, **2012**.
[20] K. Tanaka, H. Kita, M. Okano, K.-i. Okamoto, *Polymer* **1992**, *33*, 585.
[21] K. Nagai, T. Masuda, T. Nakagawa, B. D. Freeman, I. Pinnau, *Prog. Polym. Sci.* **2001**, *26*, 721.
[22] J. Rubner, L. Stellmann, A.-K. Mertens, M. Tepper, H. Roth, L. Kleines, R. Dahlmann, M. Wessling, *Plasma Processes Polym.* **2022**, *19*, 2200016.
[23] N. B. Pramanik, S. L. Regen, *Langmuir* **2020**, *36*, 1768.
[24] L. Mai, D. Maniar, F. Zysk, J. Schöbel, T. D. Kühne, K. Loos, A. Devi, *Dalton Trans.* **2022**, *51*, 1384.
[25] J. P. McCullough, J. F. Messerly, R. T. Moore, S. S. Todd, *J. Phys. Chem.* **1963**, *67*, 677.
[26] M. Deilmann, S. Theiß, P. Awakowicz, *Surf. Coat. Technol.* **2008**, *202*, 1911.
[27] R. P. Padbury, J. S. Jur, *Langmuir* **2014**, *30*, 9228.
[28] G. Golubev, S. Sokolov, T. Rokhmanka, S. Makaev, I. Borisov, S. Khashirova, A. Volkov, *Polymers* **2022**, *14*, 2944.
[29] A. Volkov, S. Tsarkov, A. Gilman, V. Khotimsky, V. Roldughin, V. Volkov, *Adv. Colloid Interface Sci.* **2015**, *222*, 716.
[30] D. S. Finch, T. Oreskovic, K. Ramadurai, C. F. Herrmann, S. M. George, R. L. Mahajan, *J. Biomed. Mater. Res., Part A* **2008**, *87A*, 100.
[31] K. H. Yoon, H. Kim, Y.-E. K. Lee, N. K. Shrestha, M. M. Sung, *RSC Adv.* **2017**, *7*, 5601.
[32] J. Jeon, D. Choi, H. Kim, Y. T. Park, M.-J. Choi, K.-B. Chung, *J. Korean Phys. Soc.* **2016**, *68*, 1024.
[33] I. Liascukiene, N. Aissaoui, S. J. Asadauskas, J. Landoulsi, J.-F. Lambert, *Langmuir* **2012**, *28*, 5116.
[34] R. G. Pearson, *J. Chem. Educ.* **1968**, *45*, 581.
[35] R. G. Pearson, *J. Chem. Educ.* **1968**, *45*, 643.
[36] C. H. Henrickson, D. P. Eyman, *Inorg. Chem.* **1967**, *6*, 1461.
[37] Y. Ren, E. K. McGuinness, C. Huang, V. R. Joseph, R. P. Lively, M. D. Losego, *Chem. Mater.* **2021**, *33*, 5210.
[38] S. Pasynkiewicz, *Pure Appl. Chem.* **1972**, *30*, 509.
[39] T. Yoshida, E. Negishi, *J. Am. Chem. Soc.* **1981**, *103*, 4985.
[40] S. Xu, E.-i. Negishi, *Acc. Chem. Res.* **2016**, *49*, 2158.
[41] V. L. Khodzhaeva, V. G. Zaikin, *J. Appl. Polym. Sci.* **2006**, *103*, 2523.
[42] W. Peng, P. Roy, L. Favaro, E. Amzallag, J. Brubach, A. Congeduti, M. Guidi-Cestelli, A. Huntz, J. Barros, R. Tétot, *Acta Mater.* **2011**, *59*, 2723.
[43] M. Nieminen, L. Niinstö, R. Lappalainen, *Microchim. Acta* **1995**, *119*, 13.
[44] I. Giner, B. Torun, Y. Han, B. Duderija, D. Meinderink, A. G. Orive, T. de los Arcos, C. Weinberger, M. Tiemann, H.-J. Schmid, G. Grundmeier, *Appl. Surf. Sci.* **2019**, *475*, 873.
[45] A. Svatoš, A. B. Attygalle, *Anal. Chem.* **1997**, *69*, 1827.
[46] J. P. Merrick, D. Moran, L. Radom, *J. Phys. Chem. A* **2007**, *111*, 11683.
[47] C. Hoppe, F. Mitschker, I. Giner, T. de los Arcos, P. Awakowicz, G. Grundmeier, *J. Phys. D: Appl. Phys.* **2017**, *50*, 204002.
[48] K. D. Dorkenoo, P. H. Pfromm, *Macromolecules* **2000**, *33*, 3747.
[49] W. Ogieglo, G. Genduso, J. Rubner, J. Hofmann-Préveraud de Vaumas, M. Wessling, I. Pinnau, *Macromolecules* **2020**, *53*, 8765.
[50] D. Nečas, P. Klapetek, *Open Phys.* **2012**, *10*, 181.
[51] E. Huang, A. Skoufis, T. Denning, J. Qi, R. Dagastine, R. Tabor, J. Berry, *J. Open Source Soft.* **2021**, *6*, 2604.
[52] C. M. Herzinger, B. Johs, W. A. McGahan, J. A. Woollam, W. Paulson, *J. Appl. Phys.* **1998**, *83*, 3323.
[53] S. Wilski, M. Jaritz, L. Kleines, R. Dahlmann, C. Hopmann, *J. Phys. D: Appl. Phys.* **2020**, *53*, 325305.
[54] L. Kleines, M. Jaritz, S. Wilski, J. Rubner, M. Alders, M. Wessling, C. Hopmann, R. Dahlmann, *J. Phys. D: Appl. Phys.* **2020**, *53*, 445301.
[55] S. Koester, F. Roghmans, M. Wessling, *J. Membr. Sci.* **2015**, *485*, 69.
[56] J. VandeVondele, M. Krack, F. Mohamed, M. Parrinello, T. Chassaing, J. Hutter, *Comput. Phys. Commun.* **2005**, *167*, 103.
[57] T. D. Kühne, M. Iannuzzi, M. Del Ben, V. V. Rybkin, P. Seewald, F. Stein, T. Laino, R. Z. Khaliullin, O. Schütt, F. Schiffmann, D. Golze, J. Wilhelm, S. Chulkov, M. H. Bani-Hashemian, V. Weber, U. Borštnik, M. Taillefumier, A. S. Jakobovits, A. Lazzaro, H. Pabst, T. Müller, R. Schade, M. Guidon, S. Andermatt, N. Holmberg, G. K. Schenter, A. Hehn, A. Bussy, F. Belleflamme, G. Tabacchi, et al., *J. Chem. Phys.* **2020**, *152*, 194103.
[58] S. Grimme, J. Antony, S. Ehrlich, H. Krieg, *J. Chem. Phys.* **2010**, *132*, 154104.
[59] S. Ehrlich, J. Moellmann, W. Reckien, T. Bredow, S. Grimme, *ChemPhysChem* **2011**, *12*, 3414.
[60] J. P. Perdew, K. Burke, M. Ernzerhof, *Phys. Rev. Lett.* **1996**, *77*, 3865.
[61] J. VandeVondele, J. Hutter, *J. Chem. Phys.* **2007**, *127*, 114105.
[62] S. Goedecker, M. Teter, J. Hutter, *Phys. Rev. B* **1996**, *54*, 1703.
[63] M. Hanwell, D. Curtis, D. Lonie, *J. Cheminform* **2012**, *4*, 1.
[64] M. Thomas, M. Brehm, R. Fligg, P. Vöhringer, B. Kirchner, *Phys. Chem. Chem. Phys.* **2013**, *15*, 6608.